Commun. Comput. Phys.
doi: 10.4208/cicp.311009.020910s

Vol. **9**, No. 5, pp. 1179-1192
May 2011

Behaviors of Spherical and Nonspherical Particles in a Square Pipe Flow

Takaji Inamuro[1,2,*], Hirofumi Hayashi[1] and Masahiro Koshiyama[1]

[1] *Department of Aeronautics and Astronautics, Graduate School of Engineering, Kyoto University, Kyoto 606-8501, Japan.*
[2] *Advanced Research Institute of Fluid Science and Engineering, Graduate School of Engineering, Kyoto University, Kyoto 606-8501, Japan.*

Received 31 October 2009; Accepted (in revised version) 2 September 2010

Available online 28 January 2011

Abstract. The lattice Boltzmann method (LBM) for multicomponent immiscible fluids is applied to the simulations of solid-fluid mixture flows including spherical or nonspherical particles in a square pipe at Reynolds numbers of about 100. A spherical solid particle is modeled by a droplet with strong interfacial tension and large viscosity, and consequently there is no need to track the moving solid-liquid boundary explicitly. Nonspherical (discoid, flat discoid, and biconcave discoid) solid particles are made by applying artificial forces to the spherical droplet. It is found that the spherical particle moves straightly along a stable position between the wall and the center of the pipe (the Segré-Silberberg effect). On the other hand, the biconcave discoid particle moves along a periodic helical path around the center of the pipe with changing its orientation, and the radius of the helical path and the polar angle of the orientation increase as the hollow of the concave becomes large.

AMS subject classifications: 76D99, 76M28, 76T99, 76Z05

Key words: Lattice Boltzmann method, square pipe flow, spherical particle, biconcave discoid particle.

1 Introduction

Solid-fluid mixture flows are of interest not only in many engineering fields such as the handling of slurry, colloid, and ceramics, but also in biological fields in connection with blood flows in capillaries. In particular, the behaviors of nonspherical particles in a pipe flow are important in relation to the motions of red blood cells in blood flows. So far, the motions of spherical particles in a pipe flow have been investigated experimentally, theoretically, and numerically by many researchers.

*Corresponding author. *Email address:* inamuro@kuaero.kyoto-u.ac.jp (T. Inamuro)

A particularly important experimental study on the motion of spherical particles in a pipe flow was performed by Segré and Siliberberg [1]. They discovered that neutrally buoyant particles in a pipe flow migrate laterally away both from the wall and the centerline and reach a certain equilibrium lateral position. Karnis et al. [2] verified the same phenomenon and observed that particles stabilize midway between the centerline and the wall, closer to the wall for larger flow rates and closer to the center for larger particles. They deduced that these phenomena are due to an inertia effect of the flow. Tachibana [3] found experimentally that the lateral migration of spheres in pipe flows depends mainly on the ratio of sphere diameter to the pipe diameter and that the phenomenon is clearly observed if this ratio exceeds about 0.2.

On the theoretical side, perturbation theories have been used to understand the lateral migration. Saffman [4] obtained the lift on a sphere particle in a shear flow in an unbounded domain. Ho and Leal [5] and Vasseur and Cox [6] investigated the lateral migration of a spherical particle in both a Couette flow and a plane Poiseuille flow bounded by two infinite plane walls. These theories for the bounded domain are valid for small channel Reynolds numbers. Schonberg and Hinch [7] extended Saffman's analysis to a small sphere in a Poiseuille flow for the channel Reynolds number of order unity, and McLaughlin [8] studied the lift on a small sphere in wall-bounded linear shear flows for small particle Reynolds numbers. Asmolov [9] investigated the inertial migration of a small rigid sphere translating parallel to the walls within a channel flow at large channel Reynolds numbers. In general, however, these perturbation theories can represent the motion of particles only subject to the severe restrictions that the Reynolds numbers be small and/or the particles be small, compared with the channel width.

On the other hand, numerical simulations have been used for the problem of particle motion in shear flows. Direct numerical simulations require no restrictions such as small Reynolds numbers, small particles, and so on. Thus, it is possible to compute the motion of particles not only around the center of a channel but also near a wall at various Reynolds numbers. Feng et al. [10] investigated the motion of a circular particle in a Couette and Poiseuille flow using a finite-element method and obtained qualitative agreement with the results of perturbation theories and of experiments. Nirschl et al. [11] carried out three-dimensional calculations of flows around a spherical particle between two moving walls using a finite-volume method with a Chimera grid scheme, but they were not concerned about the motion of the particle. Inamuro et al. [12] investigated the motions of a single and two lines of neutrally buoyant circular cylinders between flat parallel walls using the lattice Boltzmann method (LBM). Pan and Glowinski [13] carried out the direct simulations of the motion of neutrally buoyant balls in a three-dimensional Poiseuille flow using a Lagrange multiplier based fictitious domain method. From a numerical point of view, this subject is related to a moving boundary problem, and thus there are some difficulties in dealing with moving particles in a domain. Recently, in order to avoid the difficulties of the moving boundary problem, Inamuro and Ii [14] applied the LBM for multicomponent immiscible fluids with the same density to simulations of the dispersion of aggregated particles under shear flows with the Stokes flow approxima-

tion. In their work, a spherical particle is modeled by a hard droplet with large viscosity and strong surface tension, and consequently there is no need to track the moving solid-liquid boundary explicitly.

In comparison with spherical or circular particles, there have been few studies for the behaviors of nonspherical particles in pipe flows. In the present paper, we use the method of Inamuro and Ii [14] to simulate solid-fluid mixture flows including spherical and nonspherical particles, and elucidate the difference of the behaviors between spherical and nonspherical particles in a square pipe flow.

The paper is organized as follows. In Section 2, we present the numerical method using the LBM for multicomponent immiscible fluids and examine the accuracy of the method by calculating two benchmark examples. In Section 3, we simulate solid-fluid mixture flows including spherical and nonspherical (discoid, flat discoid, and biconcave discoid) particles in a square pipe. Concluding remarks are given in Section 4.

2 Numerical method

2.1 LBM for multicomponent immiscible fluids with the same density

Non-dimensional variables are used as in [15]. In the LBM, a modeled fluid, composed of identical particles whose velocities are restricted to a finite set of N vectors $\boldsymbol{c}_i$ ($i=1,2,\cdots,N$), is considered. The fifteen-velocity model ($N=15$) is used in the present paper. The velocity vectors of this model are given by

$$\begin{aligned}&[\boldsymbol{c}_1,\boldsymbol{c}_2,\boldsymbol{c}_3,\boldsymbol{c}_4,\boldsymbol{c}_5,\boldsymbol{c}_6,\boldsymbol{c}_7,\boldsymbol{c}_8,\boldsymbol{c}_9,\boldsymbol{c}_{10},\boldsymbol{c}_{11},\boldsymbol{c}_{12},\boldsymbol{c}_{13},\boldsymbol{c}_{14},\boldsymbol{c}_{15}]\\ &=\begin{bmatrix} 0 & 1 & 0 & 0 & -1 & 0 & 0 & 1 & -1 & 1 & 1 & -1 & 1 & -1 & -1 \\ 0 & 0 & 1 & 0 & 0 & -1 & 0 & 1 & 1 & -1 & 1 & -1 & -1 & 1 & -1 \\ 0 & 0 & 0 & 1 & 0 & 0 & -1 & 1 & 1 & 1 & -1 & -1 & -1 & -1 & 1 \end{bmatrix}. \end{aligned} \tag{2.1}$$

In order to distinguish each of two components in fluid with the same density, we use an order parameter ϕ which has different constant values in each component and is changed inside the interface of two components. In the formulation of the method, the lattice kinetic scheme (LKS) [15], which is an extension method of LBMs, is used. In the LKS, macroscopic variables are calculated without particle velocity distribution functions, and thus the scheme can save computer memory. The physical space is divided into a cubic lattice, and the order parameter ϕ, the pressure $p(\boldsymbol{x},t)$, and the velocity $\boldsymbol{u}(\boldsymbol{x},t)$ of whole fluid at the lattice point $\boldsymbol{x}$ and at time t are computed as follows:

$$\phi(\boldsymbol{x},t+\Delta t)=\sum_{i=1}^{15} f_i^{eq}(\boldsymbol{x}-\boldsymbol{c}_i\Delta x,t), \tag{2.2a}$$

$$p(\boldsymbol{x},t+\Delta t)=\frac{1}{3}\sum_{i=1}^{15} g_i^{eq}(\boldsymbol{x}-\boldsymbol{c}_i\Delta x,t), \tag{2.2b}$$

$$\boldsymbol{u}(\boldsymbol{x},t+\Delta t)=\sum_{i=1}^{15}\boldsymbol{c}_i g_i^{eq}(\boldsymbol{x}-\boldsymbol{c}_i\Delta x,t), \tag{2.2c}$$

where f_i^{eq} and g_i^{eq} are equilibrium distribution functions, Δx is a spacing of the cubic lattice, and Δt is a time step during which the particles travel the lattice spacing.

The equilibrium distribution functions in (2.2a), (2.2b) and (2.2c) are given by

$$f_i^{eq}=H_i\phi+F_i\Big[p_0(\phi)-\kappa_f\phi\nabla^2\phi-\frac{\kappa_f}{6}|\nabla\phi|^2\Big]+3E_i\phi c_{i\alpha}u_\alpha+E_i\kappa_f G_{\alpha\beta}(\phi)c_{i\alpha}c_{i\beta}, \tag{2.3a}$$

$$g_i^{eq}=E_i\Big[3p+3c_{i\alpha}u_\alpha-\frac{3}{2}u_\alpha u_\alpha+\frac{9}{2}c_{i\alpha}c_{i\beta}u_\alpha u_\beta+A\Delta x\Big(\frac{\partial u_\beta}{\partial x_\alpha}+\frac{\partial u_\alpha}{\partial x_\beta}\Big)c_{i\alpha}c_{i\beta}\Big]$$
$$+E_i\kappa_g G_{\alpha\beta}(\phi)c_{i\alpha}c_{i\beta}, \tag{2.3b}$$

where

$$E_1=\frac{2}{9},\quad E_2=E_3=E_4=\cdots=E_7=\frac{1}{9},\qquad E_8=E_9=E_{10}=\cdots=E_{15}=\frac{1}{72}, \tag{2.4a}$$

$$H_1=1,\quad H_2=H_3=H_4=\cdots=H_{15}=0,\quad F_1=-\frac{7}{3},\ F_i=3E_i\ \ (i=2,3,4,\cdots,15), \tag{2.4b}$$

and

$$G_{\alpha\beta}(\phi)=\frac{9}{2}\frac{\partial\phi}{\partial x_\alpha}\frac{\partial\phi}{\partial x_\beta}-\frac{3}{2}\frac{\partial\phi}{\partial x_\gamma}\frac{\partial\phi}{\partial x_\gamma}\delta_{\alpha\beta}, \tag{2.4c}$$

with $\alpha,\beta,\gamma=x,y,z$ (subscripts α,β, and γ represent Cartesian coordinates and the summation convention is used). In the above equations, $\delta_{\alpha\beta}$ is the Kronecker delta, κ_f is a constant parameter determining the width of the interface, κ_g is a constant parameter determining the strength of the surface tension, and A is a constant parameter related to fluid viscosity as shown below. In (2.3a), $p_0(\phi)$ is given by

$$p_0(\phi)=\phi T_\phi\frac{1}{1-b\phi}-a\phi^2, \tag{2.5}$$

where a,b, and T_ϕ are free parameters determining the maximum and minimum values of the order parameter, $\phi_{\max}$ and $\phi_{\min}$, respectively.

The kinematic viscosity ν and the surface tension σ are given by

$$\nu=\Big(\frac{1}{6}-\frac{2}{9}A\Big)\Delta x, \tag{2.6}$$

$$\sigma=\kappa_g\int_{-\infty}^{\infty}\Big(\frac{\partial\phi}{\partial\xi}\Big)^2 d\xi, \tag{2.7}$$

with ξ being the coordinate normal to the interface.

Note that the formulation of the method is the same as in [14] except that we include two terms with the square of the fluid velocity in (2.3b) in order to simulate flows at finite Reynolds numbers. In the following calculations, the parameters are fixed at $a=9/49$, $b=2/21$, $T_\phi=0.55$ ($\phi_{\max}=4.937$ and $\phi_{\min}=2.251$), $\kappa_f=0.01(\Delta x)^2$ and $\kappa_g=0.02(\Delta x)^2$.

2.2 Spherical and nonspherical particle models

A spherical particle is modeled by a droplet with large viscosity and strong surface tension; namely, the region where $\phi \geq (\phi_{\max}+\phi_{\min})/2$ is assigned to the droplet, and the region where $\phi < (\phi_{\max}+\phi_{\min})/2$ is assigned to a surrounding fluid. The viscosities of the droplet and the fluid are set at $\nu_{\rm p}=\Delta x/6$ and $\nu_{\rm f}=\Delta x/60$, respectively, and the viscosity inside the interface is interpolated by a liner function of ϕ as follows:

$$\nu=\nu_{\rm f}+\frac{\phi-\phi_{\max}}{\phi_{\max}-\phi_{\min}}(\nu_{\rm p}-\nu_{\rm f}). \tag{2.8}$$

On the other hand, nonspherical particles are made by applying artificial forces to the droplet. As shown in Fig. 1, we get a discoid particle by applying a centrifugal force, and also we can make a biconcave discoid particle by applying a compression force to the discoid particle. In Section 3.2, a constant centrifugal force is applied in the region of $r \geq D_{\rm p}/2$ where r is and $D_{\rm p}$ is, and a constant compression force is applied in the region of $r < D_{\rm p}/2$. It should be noted for the nonspherical particle models that in applying the artificial forces it is necessary to specify an axis initially, but the direction of the axis is changed with the motion of the particle. We calculate the eigenvectors of the inertia tensor of the particle at every time step by using the Jacobi method (see for example [16]) in order to track the direction of the axis. In addition, the total force and the total moment of the artificial forces are kept zero by redistributing a small unbalanced portion of the artificial forces inside the particle at every time step.

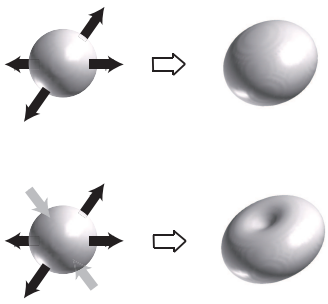

Figure 1: Artificial forces and nonspherical particles.

2.3 Accuracy of the method

To examine the accuracy of the method, we calculated two benchmark examples. The first one is a two-dimensional flow past a line of circular cylinders placed at the middle of a straight channel. Aidun and Lu [17] computed the same flow using both a finite-element method and a lattice Boltzmann method. We consider the case where the cylinders are fixed and the channel walls move tangentially with a constant velocity $u_{\rm w}$. The domain is divided into $128 \times 128 \times 1$ lattice grid and the Reynolds number is set at $Re=u_{\rm w}D_{\rm s}/\nu=1$,

where D_s is the diameter of the cylinder and ν is the kinematic viscosity of the fluid. The periodic boundary condition with zero pressure gradient is used at the inlet and outlet of the channel. We compare the results of the dimensionless force unit area of the cylinder surface $f_c = F/\pi\rho u_w^2 D_s$ (where F is the force acting on the cylinder) with those by Aidun and Lu [17] and Inamuro et al. [12] in Table 1. It is found that the present results agree well with those of the LBMs in [17] and [12] both for $D_s = 20.8\Delta x$ and $D_s = 60.8\Delta x$. In the present simulations, D_s is defined by measuring the diameter of the circular region where $\phi \geq (\phi_{max}+\phi_{min})/2$.

Table 1: Comparison of the results by the present method with those by Aidun and Lu [17] and Inamuro et al. [12] for the problem of a flow over a line of circular cylinders with a diameter D_s in a moving straight channel with a constant velocity u_w. The domain divided into 128 $\times$ 128 lattice grid. FEM and LBM[1] are results with a finite-element method and with a lattice Boltzmann method [17], respectively, and LBM[2] is a result with a lattice Boltzmann method [12]. f_c is the dimensionless force per unit area of the cylinder surface. Error is evaluated based on the result by FEM.

Case	Method	u_w	$\nu/\Delta x$	f_c	Error(%)
I ($D_s = 20.8\Delta x$)	FEM	2.00×10^{-2}	0.416	1.158	–
	LBM[1]	2.00×10^{-2}	0.416	1.229	6.1
	LBM[2]	2.00×10^{-2}	0.416	1.251	8.0
	Present	8.01×10^{-4}	1/60	1.231	6.3
II ($D_s = 60.8\Delta x$)	FEM	1.00×10^{-2}	0.608	2.067	–
	LBM[1]	1.00×10^{-2}	0.608	2.054	-0.6
	LBM[2]	1.00×10^{-2}	0.608	2.093	1.3
	Present	2.74×10^{-4}	1/60	2.042	-1.2

The second example is a sphere particle settling in a box which was measured using a PIV system by ten Cate et al. [18] and computed using an immersed boundary LBM by Feng and Michaelides [19]. The box dimensions of are $100\times100\times160$ mm (depth $\times$ width $\times$ height). The particle starts its motion at a height $h = 120$ mm from the bottom. We take the case E4 in their papers; namely, the fluid density is ρ_f =970 kg/m^3, the fluid viscosity μ_f=0.058 Ns/m^2, the sedimentation velocity of a sphere in an infinite domain is u_∞ = 0.128 m/s, the particle diameter is d_p = 15 mm, and the particle density is ρ_p = 1120 kg/m^3. In this case the Reynolds number is $Re = \rho_f u_\infty d_p/\mu_f$=31.9. The domain is divided into 200 $\times$ 200 $\times$ 320 lattice grid. Hence, the particle diameter is $30\Delta x$. The gravitational force due to the density difference between the fluid and the particle is considered by adding a body force term to the right-hand side of (2.2c) as in [15]. Fig. 2 shows the trajectory h/d_p and velocity u/u_∞ of the particle. In Fig. 2, two results calculated with the different definition of the particle diameter are shown. One result (Case 1) is obtained with the particle diameter measured in the region of $\phi \geq (\phi_{max}+\phi_{min})/2$, and the other result (Case 2) is obtained with the diameter of the region of $\phi \geq (\phi_{max}+3\phi_{min})/4$. It is seen that the result of Case 2 agrees well with the simulation in [19], while the result of Case 1 differs a little.

From the above benchmark calculations, it is found that by using the present method

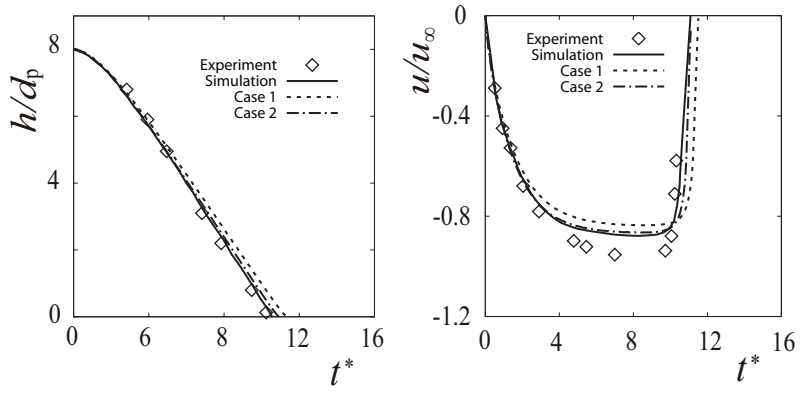

Figure 2: Comparison of the results by the present method with those by ten Cate [18] and Feng and Michaelides [19] for a sphere particle settling in a box. The trajectory h/d_p (left) and the velocity u/u_∞ (right) of the particle are shown. The symbol $\diamond$ is the result in [18], the solid line is the result in [19]. Case 1 is the result obtained with the particle diameter measured in the region of $\phi \geq (\phi_{max}+\phi_{min})/2$, and Case 2 is the result obtained with the diameter of the region of $\phi \geq (\phi_{max}+3\phi_{min})/4$. The dimensionless time is defined by $t^* = u_\infty t/d_p$.

we can simulate the behavior of a solid particle in a fluid within the errors of a few percent compared with the results by other numerical methods.

3 Results and discussion

We consider solid-fluid mixture flows including spherical and nonspherical particles in a square pipe with the width of D and the length of L_x as shown in Fig. 3. The domain is divided into $120 \times 60 \times 60$ cubic lattice in the x-, y-, and z-directions. The no-slip boundary condition proposed in [20] is used on the side walls, and the periodic boundary condition with a pressure difference Δp proposed in [21] is used at the inlet ($x = 0$) and the outlet ($x = L_x$). In addition, the Reynolds number is defined by $Re = VD/\nu_f$ where V is the averaged velocity at the inlet after a steady flow is obtained.

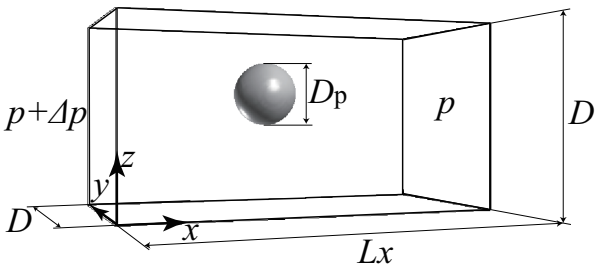

Figure 3: Computational domain and a particle.

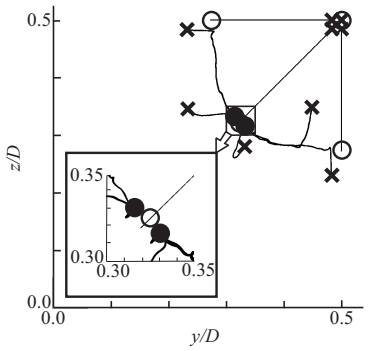

Figure 4: Trajectories and equilibrium positions of a spherical particle on the yz plane; $\times$, initial positions; $\bullet$, stable equilibrium positions; $\circ$, unstable equilibrium positions. The region of $0.3 \leq y/D \leq 0.35$ and $0.3 \leq z/D \leq 0.35$ is zoomed.

3.1 Spherical particle

First, a spherical particle is put at a certain position in the domain, and a pressure difference Δp is applied between the inlet and the outlet at $t = 0$. It is noted that we consider a line of spherical particles in a long square pipe. The ratio of the particle diameter to the pipe width is $D_p/D = 1/3$. The volume fraction H_t of the particle in the domain is $H_t = 0.0097$. The Reynolds numbers is $Re = 106$. Fig. 4 shows the trajectories of the mass center and the equilibrium positions of the particle released at nine different initial positions on the yz-plane. Considering the symmetry of the domain, we choose the initial positions in a quarter domain. We have calculated particle trajectories from many different initial positions, and the typical nine results of those are shown in Fig. 4. In the figure, the symbol $\times$ shows the initial positions, the symbol $\bullet$ indicates stable equilibrium positions, and the symbol $\circ$ indicates unstable equilibrium positions where the particle released from the special initial positions ($y/D = 0.5$, $z/D = 0.5$, and $y = z$) reaches, but the particle moves to the stable equilibrium position by a small disturbance. It is found that two stable equilibrium positions exist at $(y/D, z/D) = (0.317, 0.332)$ and $(0.332, 0.317)$ in the quarter domain. The spherical particle moves straightly in the x-direction at the stable equilibrium position on the yz-plane. These results correspond to the Segré-Silberberg effect [1].

3.2 Nonspherical particles

Three nonspherical particles shown in Fig. 5 are considered. Model 1 is a discoid particle, Model 2 is a flat discoid particle, and Model 3 is a biconcave discoid particle. We made Model 1, Model 2, and Model 3 with the centrifugal force of 3.0×10^{-4} and with the compression forces of 1.5×10^{-4}, 3.0×10^{-4}, and 4.5×10^{-4}, respectively, as explained in Section 2.2. Computational conditions are $H_t = 0.017$ and $Re = 107$ for all the cases.

First, calculated results for the discoid particle (Model 1) are shown in Figs. 6 and 7. Fig. 6 shows the motion of the particle. Fig. 7 shows the variations of the position of

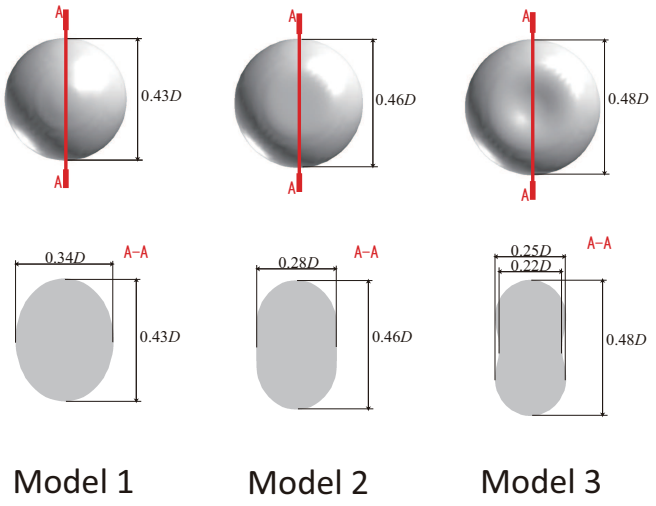

Figure 5: Nonspherical particles; discoid (Model 1), flat discoid (Model 2), and biconcave discoid (Model 3).

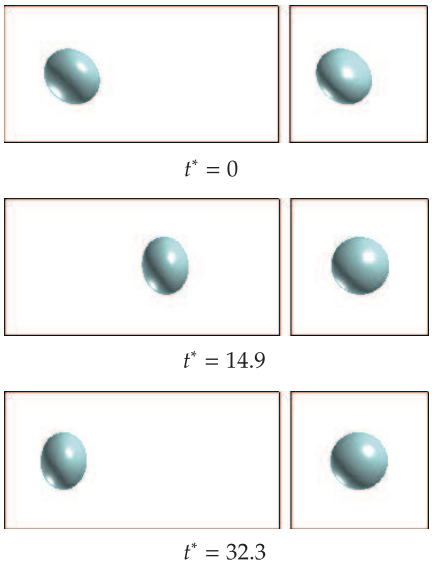

Figure 6: The motion of a discoid particle (Model 1); side view from $y=-\infty$ (left) and front view from $x=\infty$ (right). $t^*=Vt/L_x$ where V is the averaged velocity at the inlet after a steady flow is obtained.

the mass center in the y- and z-directions and the variations of the polar angle θ and of the azimuthal angle φ of the minor axis of the discoid particle. With taking the X-axis as the polar axis, θ and φ are defined by $\theta=\cos^{-1}(X/\sqrt{X^2+Y^2+Z^2})$ in $0\le\theta\le\pi$ and $\varphi=\tan^{-1}(Z/Y)$ in $-\pi<\varphi\le\pi$, respectively, where (X,Y,Z) are Cartesian components of the minor axis of the discoid particle measured from the mass center of the particle. It is seen from Fig. 6 that the particle moves upright along the center of the pipe after $t^*=14.9$. However, it is found from Fig. 7 that the particle moves periodically; i.e., the

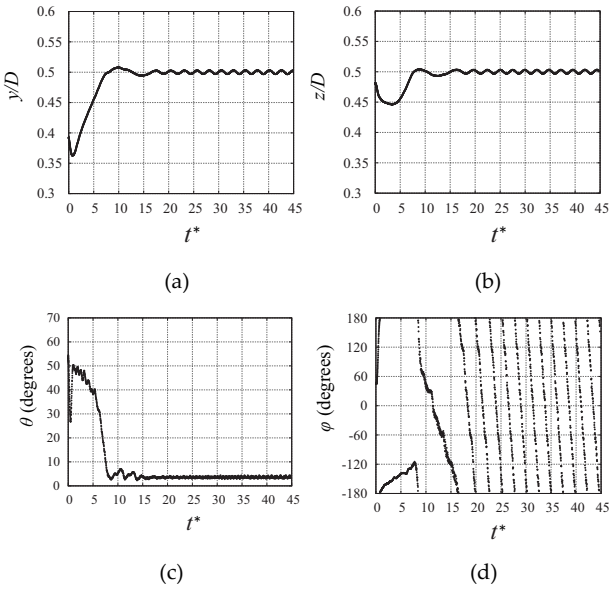

Figure 7: Time variations of a discoid particle (Model 1). (a) The y-component of the position of the mass center; (b) the z-component of the position of the mass center; (c) the polar angle θ of the minor axis of the particle; (d) the azimuthal angle φ of the minor axis of the particle.

mass center moves along a periodic helical path rotating in the negative direction along the x-axis with a small radius around the center of the pipe, and the minor axis of the particle rotates periodically in the negative direction of φ with $\theta \approx 4$ degrees. It is noted that the rotating direction of the mass center is identical with that of the minor axis of the particle. In addition, it was confirmed that the rotating direction depends on initial positions and orientations of the particle. The time averaged length and radius of the helical path and the time averaged polar angle $\overline{\theta}$ of the minor axis of the particle in a period are summarized in Table 2. The time averaged velocity of the particle in the x-direction, V_{p}, is also listed in Table 2.

Table 2: The time averaged length and radius of the helical path, the time averaged polar angle of the minor axis of the particle, $\overline{\theta}$, and the time averaged velocity of the particle in the x-direction V_{p}. The time averaged values are obtained from the data of the final three periods measured by the peaks of the z-component of the particle positions.

Model	Length	Radius	$\overline{\theta}$ (degrees)	V_{p}/V
1	$8.5D$	$0.003D$	3.6	1.78
2	$13.7D$	$0.034D$	33.5	1.74
3	$13.0D$	$0.050D$	43.6	1.68

Next, Figs. 8 and 9 show calculated results for the flat discoid particle (Model 2). It is seen from Fig. 8 that the particle moves around the center of the pipe with changing its orientation. The motion of the particle can be clearly found from Fig. 9. The particle

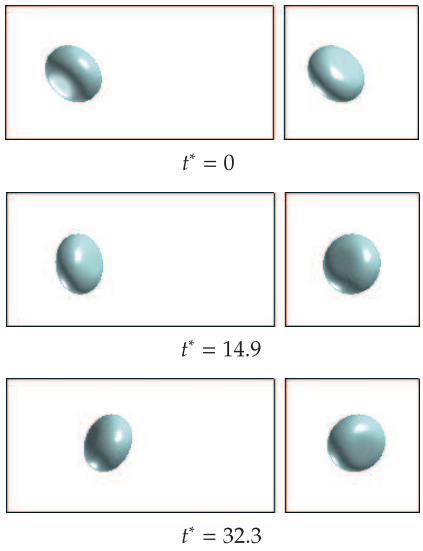

Figure 8: The motion of a flat discoid particle (Model 2); side view from $y=-\infty$ (left) and front view from $x=\infty$ (right). $t^*=Vt/L_x$ where V is the averaged velocity at the inlet after a steady flow is obtained.

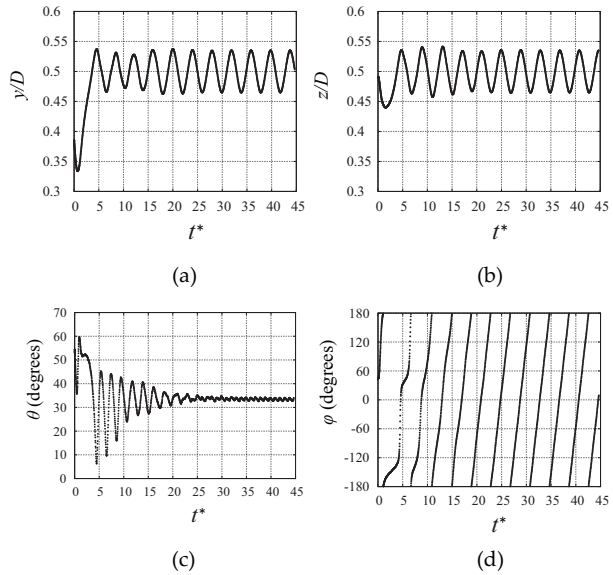

Figure 9: Time variations of a flat discoid particle (Model 2). (a) The y-component of the position of the mass center; (b) the z-component of the position of the mass center; (c) the polar angle θ of the minor axis of the particle; (d) the azimuthal angle φ of the minor axis of the particle.

moves along a periodic helical path rotating in the positive direction along the x-axis with a larger radius than Model 1. Also, the minor axis of the particle rotates periodically in the positive direction of φ with larger polar angle θ than Model 1. It is found from Fig. 9 (b) and (d) that the time of the maximum z-component of the mass center corresponds to

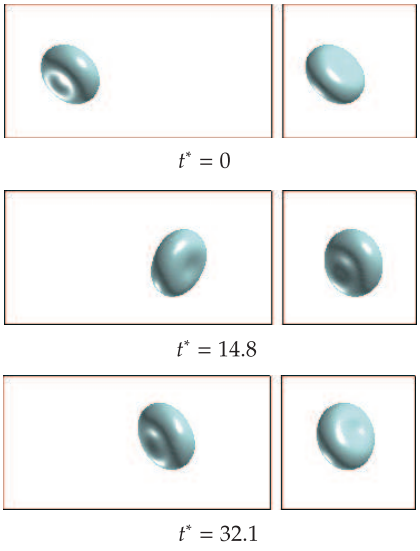

Figure 10: The motion of a biconcave discoid particle (Model 3); side view from $y=-\infty$ (left) and front view from $x=\infty$ (right). $t^*=Vt/L_x$ where V is the averaged velocity at the inlet after a steady flow is obtained.

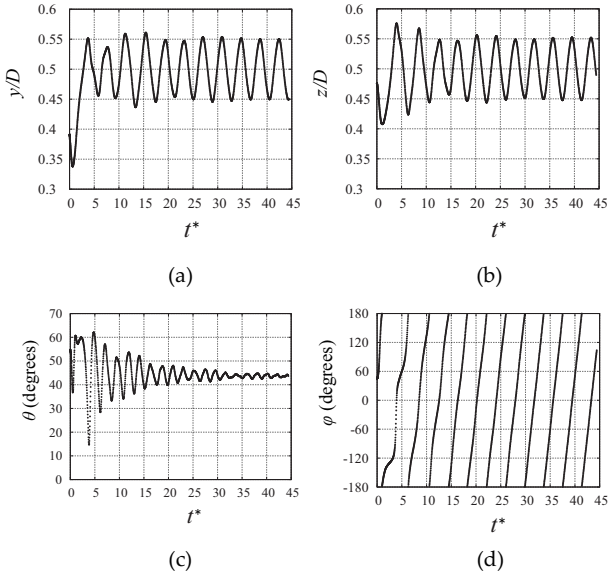

Figure 11: Time variations of a biconcave discoid particle (Model 3). (a) The y-component of the position of the mass center; (b) the z-component of the position of the mass center; (c) the polar angle θ of the minor axis of the particle; (d) the azimuthal angle φ of the minor axis of the particle.

that of $\varphi \approx 0$; it means that the phase change of φ is about 90 degrees behind that of the rotation of mass center on the yz-plane.

Finally, Figs. 10 and 11 show calculated results for the biconcave discoid particle (Model 3). The motion of the biconcave discoid particle is similar to Model 2, but both

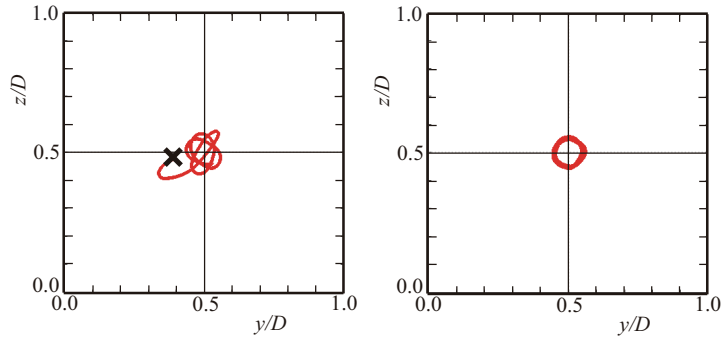

Figure 12: Trajectory of a biconcave discoid particle (Model 3). (a) $0 \leq t^* \leq 14.8$, $\times$: initial position. (b) $14.8 \leq t^* \leq 44.4$.

the radius of the helical path and the polar angle of the particle rotation are larger than Model 2. The detailed comparisons are referred to Table 1. The trajectory of the particle on the yz-plane is shown in Fig. 12. As seen in Figs. 11 and 12, the particle moves randomly in early time, but it goes along almost the same path around the center of the pipe in later time which means that the particle finally moves along a periodic helical path.

4 Concluding remarks

We have applied the LBM for multicomponent immiscible fluids to the simulations of solid-fluid mixture flows including spherical and nonspherical particles in a square pipe. It is found that spherical particles move around stable positions between the wall and the center of the pipe (the Segré-Silberberg effect). On the other hand, a biconcave discoid particle moves along a periodic helical path around the center of the pipe with changing its orientation, and the radius of the helical path and the polar angle of the orientation increase as the hollow of the concave becomes large.

Further work remains in order to clarify the fluid dynamic mechanisms of the helical motion and the rotating orientation of the biconcave discoid particle. In addition, the effect of the Reynolds number on the particle behaviors will be investigated in future work.

Acknowledgments

This work is partly supported by the Grant-in-Aid for Scientific Research (No. 18360089) from JSPS and by the COE program (the Center of Excellence for Research and Education on Complex Functional Mechanical Systems) of the Ministry of Education, Culture, Sports, Science and Technology, Japan.

References

[1] G. Segré, and A. Silberberg, Radial particle displacements in Poiseuille flow of suspensions, Nature., 189 (1961), 209–210.
[2] A. Karnis, H. L. Goldsmith, and S. G. Mason, The flow of suspensions through tubes, Can. J. Chem. Eng., 44 (1966), 181–193.
[3] M. Tachibana, On the behavior of a sphere in the laminar tube flows, Rheol. Acta., 12 (1973), 58–69.
[4] P. G. Saffman, The lift on a small sphere in a slow shear flow, J. Fluid. Mech., 22 (1965), 385–400.
[5] B. P. Ho, and L. G. Leal, Inertial migration of rigid spheres in two-dimensional unidirectional flows, J. Fluid. Mech., 35 (1974), 365–400.
[6] P. Vasseur, and R. G. Cox, The lateral migration of a spherical particle in two-dimensional shear flows, J. Fluid. Mech., 78 (1976), 385–413.
[7] J. A. Schonberg, and E. J. Hinch, Inertial migration of a sphere in Poiseuille flow, J. Fluid. Mech., 203 (1989), 517–524.
[8] J. B. McLaughlin, The lift on a small sphere in wall-bounded linear shear flows, J. Fluid. Mech., 246 (1993), 249–265.
[9] E. S. Asmolov, The iniertial lift on a spherical particle in a plane Poiseuiile flow at large channel Reynolds number, J. Fluid. Mech., 381 (1999), 63–87.
[10] J. Feng, H. H. Hu, and D. D. Joseph, Direct simulation of initial value problems for the motion of solid bodies in a Newtonian fluid, part 2: Couette and Poseuille flows, J. Fluid. Mech., 277 (1994), 271–301.
[11] H. Nirschl, H. A. Dwyer, and V. Denk, Three-dimensional calculations of the simple shear flow around a single particle between two moving walls, J. Fluid. Mech., 283 (1995), 273–285.
[12] T. Inamuro, K. Maeba, and F. Ogino, Flow between parallel walls containing the lines of neutrally buoyant circular cylinders, Int. J. Multiphase. Flow., 26 (2000), 1981–2004.
[13] T. W. Pan, and R. Glowinski, Direct simulation of the motion of neutrally buoyant balls in a three-dimensional Poiseuille flow, C. R. Mecanique., 333 (2005), 884–895.
[14] T. Inamuro, and T. Ii, Lattice Boltzmann simulation of the dispersion of aggregated particles under shear flows, Math. Comput. Sim., 72 (2006), 141–146.
[15] T. Inamuro, Lattice Boltzmann methods for viscous fluid flows and for two-phase fluid flows, Fluid. Dyn. Res., 38 (2006), 641–659.
[16] W. H. Press, B. P. Flannery, S. A. Teukolsky, and W. T. Vetterling, Jacobi Transformations of A Symmetric Matrix, in Numerical Recipes (FORTRAN Version), Cambridge University Press, 1989.
[17] C. K. Aidun, and Y. Lu, Lattice Boltzmann simulation of solid particles suspended in fluid, J. Stat. Phys., 81 (1995), 49–61.
[18] A. ten Cate, C. H. Nieuwstad, J. J. Derksen, and H. E. A. Van den Akker, Particle imaging velocimetry experiments and lattice-Boltzmann simulations on a single sphere settling under gravity, Phys. Fluids., 14 (2002), 4012–4025.
[19] Z.-G. Feng, and E. E. Michaelides, Proteus: a direct forcing method in the simulations of particulate flows, J. Comput. Phys., 202 (2005), 20–51.
[20] T. Inamuro, M. Yoshino, and F. Ogino, A non-slip boundary condition for lattice Boltzmann simulations, Phys. Fluids., 7 (1995), 2928–2930 (Erratum: 8 (1996) 1124).
[21] T. Inamuro, M. Yoshino, and F. Ogino, Lattice Boltzmann simulation of flows in a three-dimensional porous structure, Int. J. Numer. Meth. Fluids., 29 (1999), 737–748.